RSC Advances

PAPER

View Article Online
View Journal | View Issue

Cite this: *RSC Adv.*, 2025, **15**, 37050

Study on the structural, optical, vibrational and dielectric properties of Cr^{2+}-doped $SnFe_2O_4$ spinel ferrites

Abid Zaman, *[a] Asad Ali, *[b] Hifsa Shahid,[c] Salhah Hamed Alrefaee,[d] Salah Knani,*[e] Vineet Tirth,[fg] Ali Algahtani[fh] and Noureddine Elboughdiri [i]

Received 18th July 2025
Accepted 22nd September 2025

DOI: 10.1039/d5ra05190h

rsc.li/rsc-advances

Herein, we have examined the effects of Cr^{2+} doping on the structural, optical, microstructural, and dielectric properties of $SnFe_2O_4$ spinel ferrites prepared by the conventional solid-state route. X-ray diffractometry (XRD) analysis confirmed the formation of a single-phase cubic spinel structure with the space group $Pn\bar{3}$. A decrease in the lattice parameters and crystallite size was observed with increasing Cr^{2+} content. Scanning electron microscopy (SEM) revealed a homogeneous and densely packed microstructure with a reduced grain size upon Cr^{2+} doping. The optical band gap energies, as measured by UV-vis spectrometry, were observed to decrease from 2.58 eV to 2.32 eV. Fourier transform infrared (FTIR) spectrometry revealed subtle modifications in the metal–oxygen (M–O) vibrational bands due to Cr^{2+} doping. Frequency and concentration (x) also significantly influenced the dielectric properties of the synthesized samples. An improved resistive grain boundary behavior and less space charge polarization were indicated by a significant decrease in $\tan\delta$ and an improvement in frequency stability, respectively, as the concentration of Cr^{2+} increased. With increasing Cr^{2+} content, a decrease in σ_{ac} was observed, which in turn reduced both the leakage current and tangent loss. The observed reduction in modulus due to doping reflects enhanced charge transport and diminished polarization, making the material suitable for use in memory devices, sensors, and spintronic components.

1. Introduction

The structural, optical, dielectric, and magnetic properties of spinel ferrites, with a general formula of AB_2O_4, (where A and B represent divalent and trivalent metal cations, respectively), make them an important family of magnetic materials. Due to its potential applications in dielectric resonator antennas, energy storage systems, magnetic storage devices, microwave absorbers, catalysis, and sensors, tin ferrite ($SnFe_2O_4$), a less explored inverse spinel, has garnered a lot of attention recently.[1–3] Appropriate doping at either the A-site or the B-site can fine-tune the performance and multifunctional properties of these ferrites by modifying their electronic structure and cation distribution. Because of chromium's distinct electronic structure ($3d^4$) and varied oxidation states, Cr^{2+} ion doping in spinel ferrites is particularly interesting. Owing to the synthesis conditions and compatibility of the ionic radii, Cr^{2+} can be introduced into the spinel lattice at tetrahedral sites. This could change the M–O super exchange interactions, which would impact the band gap, lattice vibrations, dielectric relaxation mechanisms, and overall crystal structure.[4,5] The Cr^{2+} ion (ionic radius 0.73 Å) is a good option for site-selective doping investigations since it is similar in size to Sn^{2+} and permits partial substitution without causing significant lattice deformation.[6] In its pure form, $SnFe_2O_4$ crystallizes in a cubic spinel structure in the $Fd\bar{3}m$ space group. The interactions between the tetrahedrally coordinated Sn^{2+} ions are responsible for its ferromagnetic characteristics.[7] The structural stability, optical absorption properties, vibrational modes, and dielectric behavior of Sn^{2+} are anticipated to be modulated by doping with Cr^{2+}. In comparable spinel systems, for example, Cr^{2+} doping has been demonstrated to improve the phonon confinement, decrease the optical band gap, and increase the dielectric

[a]*Department of Physics, Riphah International University, Islamabad 44000, Pakistan. E-mail: zaman.abid87@gmail.com*
[b]*Department of Physics, Government Postgraduate College, Nowshera 24100, KP, Pakistan. E-mail: kasadiiui@gmail.com*
[c]*Department of Electrical Engineering, College of Engineering, Qassim University, Unayzah, Saudi Arabia*
[d]*Department of Chemistry, College of Science Taibah University Yanbu Governorate, Saudi Arabia*
[e]*Center for Scientific Research and Entrepreneurship, Northern Border University, Arar 73213, Saudi Arabia. E-mail: saleh.kenani@nbu.edu.sa*
[f]*Mechanical Engineering Department, College of Engineering, King Khalid University, Abha 61421, Aseer, Kingdom of Saudi Arabia*
[g]*Centre for Engineering and Technology Innovations, King Khalid University, Abha 61421, Aseer, Kingdom of Saudi Arabia*
[h]*Research Center for Advanced Materials Science (RCAMS), King Khalid University, Guraiger, P.O. Box 9004, Abha 61413, Aseer, Kingdom of Saudi Arabia*
[i]*Chemical Engineering Department, College of Engineering, University of Ha'il, P. O. Box 2440, Ha'il 81441, Saudi Arabia*

constant *via* localized charge polarization. The Cr^{2+}/Cr^{3+} substitution may introduce localized states within the band gap of $SnFe_2O_4$.[8–10] These states can act as intermediate energy levels, facilitating defect-related transitions, and other relevant ferrites can influence these observed optical absorptions, and magnetic, vibrational, electrochemical, and dielectric properties.[11–13] Additionally, the physical features of spinel ferrites can provide useful data about their electrical structures and bonding characteristics. These properties are also utilized for energy storage, supercapacitors, photocatalysis, optoelectronics in the millimeter range, MRI, and environmental applications.[14–17] Fourier-transform infrared (FTIR) and Raman spectroscopy are crucial for identifying the intrinsic vibrational modes of metal–oxygen interactions at tetrahedral sites, which reveal the degree of cationic substitution and structural deformation caused by doping.[18–20] The dielectric characteristics, such as AC conductivity, tangent loss, and dielectric constant, are highly influenced by elements like defect density, grain boundaries, and hopping mechanisms between localized charge carriers. Analyzing dielectric and optoelectronics properties at various frequencies and temperatures can help one better understand the underlying polarization mechanisms and conduction phenomena that are crucial for memory device applications.[21–24]

Therefore, in this research, the effect of chromium doping in tin ferrites $Sn_{1-x}Cr_xFe_2O_4$ (where $x = 0.00$, 0.20, 0.40, and 0.60) is explored, as this doping system has not been extensively investigated in the literature. Systematic research is required to link the structural alterations brought about by Cr^{2+} substitution to the alterations in optical, vibrational, and dielectric properties that follow. This work aims to bridge that gap by synthesizing Cr^{2+}-doped $SnFe_2O_4$ ferrites by the solid-state mixed oxide technique and then fully characterizing them using FTIR, UV-vis, X-ray diffraction (XRD), and impedance spectroscopy. This study provides valuable insights into the structure–property linkages of Cr^{2+}-substituted $SnFe_2O_4$ spinel ferrites, which can be used to tailor these materials for use in electrical, photonic, and spintronic applications.

2. Materials and method

The solid-state mixed oxide method was used to create chromium-doped tin ferrite samples with the nominal composition $Sn_{1-x}Cr_xFe_2O_4$ (where $x = 0.00$, 0.20, 0.40, and 0.60).[25,26] Because of its affordability, ease of use, and capacity to produce materials with a high degree of crystallinity, this traditional ceramic method was selected. As starting materials, analytical grade oxides such as SnO (99.9%, Sigma-Aldrich), FeO_3 (99.5%, Merck), and CrO (99%, Alfa Aesar) were utilized. Using an agate mortar and pestle, these oxides were weighed in stoichiometric amounts and thoroughly combined, with acetone being used as a grinding medium to increase homogeneity. To guarantee that the reactants were completely blended, the mixing process was carried out for four to six hours. The uniform powder blends were pre-calcined in air for 6 hours at 800 °C with a heating/cooling rate of 10 °C min^{-1} to start the solid-state processes and make the formation easier. The uniform powder blends were pre-calcined in air for 06 hours at 800 °C to start solid-state reactions and help the ferrite phase develop. Following calcination, the powders were once more ground to a fine consistency before being compressed using a uniaxial hydraulic press with a 5-ton load to form round pellets of 10 mm in diameter and 5 mm in thickness. During the pelletization process, polyvinyl alcohol (PVA) was added as a temporary binder. To guarantee densification and phase stability, the pellets were further sintered for 6 hours at 950 °C using a high-energy furnace. A Bruker D8 Advance diffractometer that operated at 40 kV and 40 mA and used Cu-Kα radiation ($\lambda = 1.5406$ Å), X-ray diffraction (XRD) was used to analyze the structural characteristics of the generated samples. With a step size of 0.02°, the diffraction data were acquired throughout a 2θ range of 10°–70°. A Shimadzu UV-2600 spectrophotometer was used to conduct UV-visible spectroscopic analysis in the 200–800 nm wavelength range in order to investigate the optical absorption behavior and calculate the optical band gap energy by using Tauc plot analysis. The vibrational behaviors of the samples were analyzed using FTIR spectrometry (PerkinElmer Spectrum Two spectrometer), with spectra recorded in the range 400–4000 cm^{-1}. To ensure good electrical contact, the sintered pellets were dried at 120 °C after being covered with silver paste on both flat surfaces to serve as electrodes for dielectric characterization. The dielectric properties, *i.e.*, dielectric constant, tangent loss, AC conductivity, impedance, as well as modulus measurements, were carried out at room temperature using impedance analyzer spectroscopy.

3. Results and discussion

3.1 Phase analysis

The phase purity and crystal structures of the $Sn_{1-x}Cr_xFe_2O_4$ (where $x = 0.00$, 0.20, 0.40, and 0.60) spinel ferrites were analyzed using X-ray diffraction (XRD) patterns, verified by Bragg's angle (2θ) range of 10°–70°, as shown in Fig. 1(a and b). A single-phase cubic spinel structure along with space group ($Pn\bar{3}$) has been confirmed from the XRD data and matched with the standard JCPDS card no. 01-074-1745. The preferred orientation of the crystallites is shown by the largest intensity peak at the (200) plane. The effective substitution of Cr^{2+} ions into the $SnFe_2O_4$ spinel lattice without altering the overall structure was demonstrated by the absence of secondary phases and impurity peaks in the XRD patterns. The doped ferrites' phase stability under the applied sintering conditions is further suggested by the lack of impurity phases. Fig. 1(c) presents the Rietveld refinement profile of the prepared sample. The XRD patterns were refined using the FullProf program, which applies the space group symmetry, together with an initial structural model, to achieve the refinement.

The average crystallite size (D) was calculated by using the Debye–Scherrer formula:[27]

$$D = \frac{0.9\lambda}{\beta \cos \theta} \quad (1)$$

The calculated average crystallite size was found to be in the range of 20–36 nm, suggesting the nanocrystalline nature of the

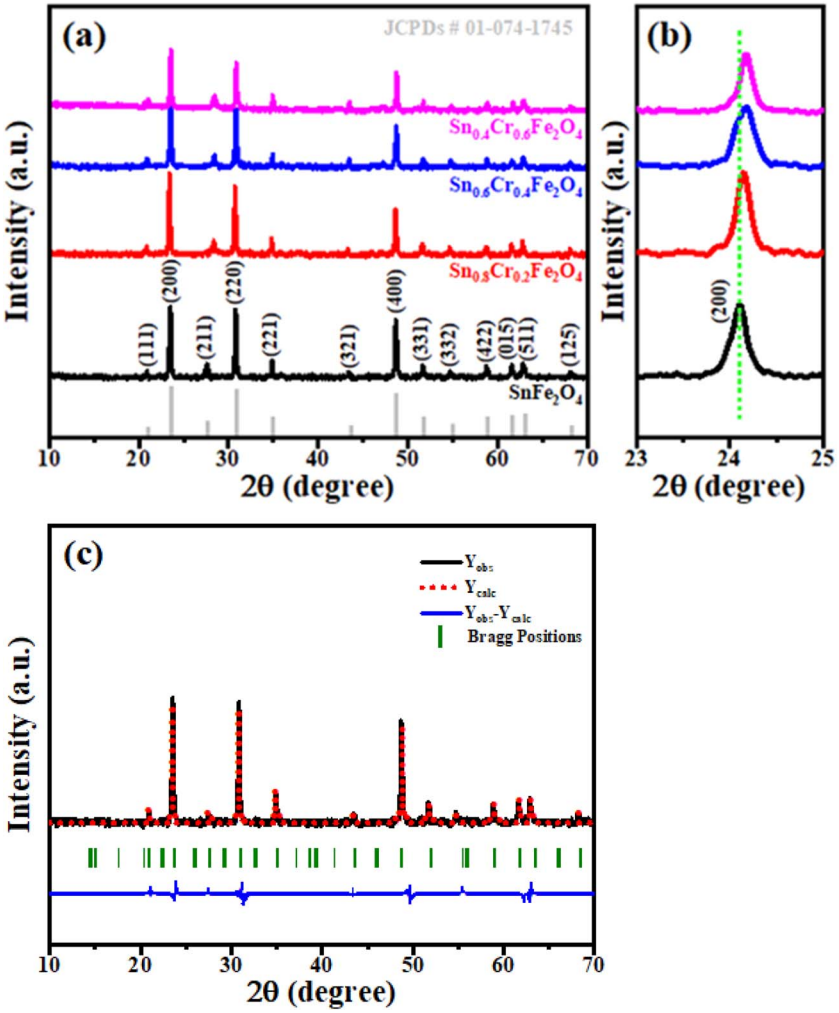

Fig. 1 (a) XRD patterns and (b) locally enlarged (200) peaks of $Sn_{1-x}Cr_xFe_2O_4$ (where $x = 0.00$, 0.20, 0.40, and 0.60). (c) Rietveld refinement of the synthesized samples using the FullProf program.

synthesized ferrites. Additionally, the lattice parameter was calculated by using the interplanar spacing formula for cubic spinel systems:

$$a = \frac{d}{\sqrt{(h^2 + k^2 + l^2)}} \quad (2)$$

The calculated lattice parameter showed a slight variation with Cr^{2+} doping, attributed to the substitution of Sn^{+} (1.22 Å) with Cr^{2+} (0.73 Å), which has a smaller ionic radius. This leads to a minor diminution of the unit cell volume.

The following formulas can be used to determine the dislocation density (δ), micro strain (ε), and lattice strain (η) for complex perovskites:[28–30]

$$\delta = \frac{1}{D^2} \quad (3)$$

$$\varepsilon = \frac{d}{D\sqrt{12}} \quad (4)$$

$$\eta = \frac{\beta \cos \theta}{4} \quad (5)$$

The estimated values of crystallite size, lattice strain, microstrain, and dislocation density are listed in Table 1. These structural parameters confirm the nanostructured and defect-rich nature of the Cr^{2+}-doped $SnFe_2O_4$ ferrites, which can significantly influence their optical and dielectric behaviors.

Table 1 Physical parameters of microstrain (ε), crystallite size (D), lattice strain (η), and dislocation density (δ) for the $Sn_{1-x}Cr_xFe_2O_4$ (where $x = 0.00$, 0.20, 0.40, and 0.60) spinel ferrites

Parameters	$x = 0.00$	$x = 0.20$	$x = 0.40$	$x = 0.60$
D (nm)	21	36	25	20
δ ($\times 10^{-3}$) nm^{-2}	2.348	0.749	1.632	2.616
η ($\times 10^{-2}$)	1.679	0.947	0.163	0.262
ε	0.1492	0.1657	0.1527	0.1655

These findings indicate that Cr^{2+} incorporation does not disrupt the spinel phase but introduces controlled microstrain and defects, which are favorable for tailoring functional properties in magnetic and dielectric applications. Similar structural behavior upon Cr^{2+} substitution in spinel ferrites has also been reported in recent literature.[31–33]

3.2 Scanning electron microscopy (SEM) analysis

The surface morphologies of $Sn_{1-x}Cr_xFe_2O_4$ (where x = 0.00, 0.20, 0.40, and 0.60) spinel ferrites were investigated using Scanning Electron Microscopy (SEM), and the representative micrographs are shown in Fig. 2. The sample has a moderate porosity and a crystalline microstructure made up of closely spaced grains with a fairly even distribution. Ferrites produced by the traditional solid-state (mixed oxide) process are characterized by predominantly round to irregular grains with some agglomeration; there is enough grain development and sintering, as evidenced by the distinct grain boundaries. The average crystallite size estimated from XRD (20–36 nm) confirms the nanocrystalline nature of the samples. The SEM images show larger grain sizes in the range of 200–600 nm, which are aggregates of these nanosized crystallites.[20] The tiny grain size is attributed to the replacement of Cr^{2+} ions at the tetrahedral sites, which may act as a grain growth inhibitor due to their different ionic radius and lower diffusion coefficient compared to Sn^{2+}. Micropores scattered across the matrix are a sign of partial densification, which could be the result of volatile components escaping during high-temperature sintering or incomplete sintering. Despite their small size, these pores may play an important role in modifying the dielectric and transport properties of the material, especially through their influence on the space charge polarization mechanism at the grain boundary interfaces.[34,35] Additionally, there is no indication of secondary phases or aberrant grain development in the microstructure, confirming the phase purity and the successful integration of Cr^{2+} ions into the spinel lattice without compromising the microstructural integrity. Reliable dielectric and magnetic performances in ferrite systems require a high degree of compositional homogeneity, which is implied by the morphological uniformity throughout the scanned region. By promoting Maxwell–Wagner interfacial polarization, the

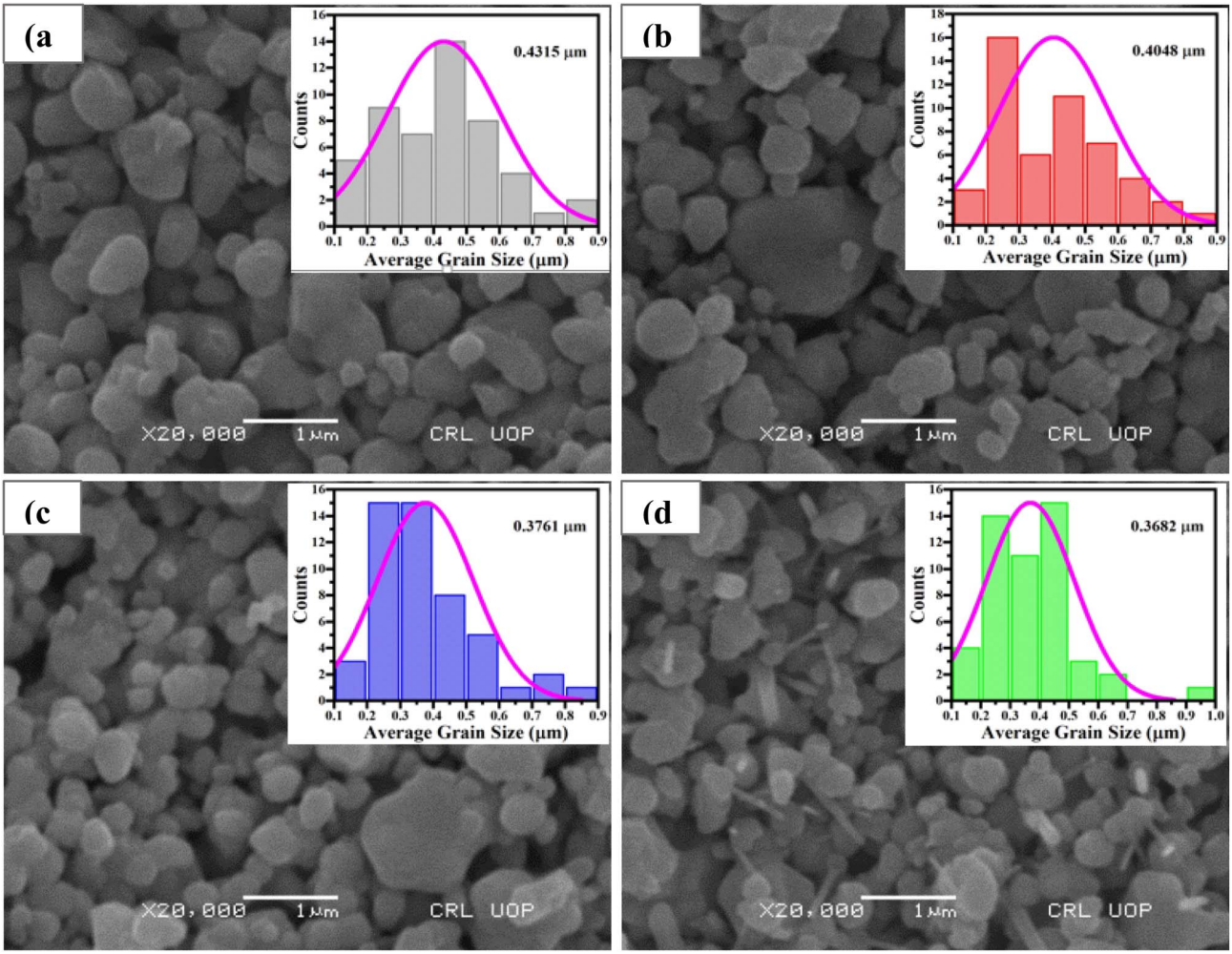

Fig. 2 SEM images of the $Sn_{1-x}Cr_xFe_2O_4$ (where x = 0.00, 0.20, 0.40, and 0.60) spinel ferrites showing the uniform grain distribution, nanograined microstructure, and presence of intergranular porosity (a) x = 0.00, (b) x = 0.20, (c) x = 0.40 and (d) x = 0.60.

comparatively tiny grain size and interconnected grain network can improve dielectric responsiveness. Additionally, the reported microstructural properties show promise for use in electromagnetic devices, where performance can be significantly impacted by controlled porosity and grain size.[36,37]

4. Optical properties

4.1 Fourier transform infrared (FTIR) spectrometry

FTIR spectrometry was employed to investigate the vibrational modes and bonding characteristics of $Sn_{1-x}Cr_xFe_2O_4$ (where x = 0.00, 0.20, 0.40, and 0.60) spinel ferrites in the range of 4000–400 cm^{-1}, as shown in Fig. 3. The spectra exhibit multiple absorption bands that confirm the formation of the spinel ferrite structure and provide insight into the local bonding environment of constituent ions. A broad absorption band observed in the region of ~3400–3200 cm^{-1} corresponds to the stretching vibrations of the O–H group, which arises due to the adsorbed moisture or hydroxyl groups present on the surface of the ferrite particles.[38] Due to variations in porosity or surface area, the intensity of this band varies slightly with the concentration of Cr^{2+} doping. The H–O–H bending vibrations of water molecules physically adsorbed on the ferrite surface are responsible for the distinctive absorption bands located between about 3000 and 3350 cm^{-1}.[39] These features confirm minor hydration, common in ferrite ceramics. The most significant and characteristic absorption bands of spinel ferrites appear in the lower wavenumber region. A strong band in the range of ~500–700 cm^{-1} is assigned to the basic stretching vibrational mode of the metal–oxygen (M–O) bond at the A-site cation. The band observed at ~1100–1600 cm^{-1} is attributed to stretching vibrations at the A-site cation, typically involving Sn–O or Cr–O bonds.[40,41] With increasing Cr^{2+} doping (x = 0.00 to 0.60), these bands show slight shifts in position and variation in intensity, indicating the substitutional incorporation of Cr^{2+} ions into the lattice and corresponding alterations in bond lengths and force constants. The Sn–O stretching vibrations are evident near ~1100–1600 cm^{-1}, showing marginal intensity modifications with Cr^{2+} content. The shift in band positions with increased doping suggests lattice distortion due to the ionic radius mismatch between Cr^{2+} (0.73 Å) and Sn^{2+} (1.22 Å), supporting the successful incorporation of Cr^{2+} ions into the spinel framework.[42] Overall, the FTIR spectra confirmed the formation of a single-phase spinel ferrite structure with Cr^{2+} ions effectively replacing Sn^{2+} or occupying the A-site cation position.

4.2 Photoluminescence (PL) spectrophotometry

PL spectrophotometry is an effective method for examining the optical characteristics of semiconductors or electrical insulator materials. Fig. 4 shows the PL spectra of the $Sn_{1-x}Cr_xFe_2O_4$ (where x = 0.00, 0.20, 0.40, and 0.60) spinel ferrites. Every sample was stimulated under identical conditions to ensure uniformity. A single broad emission peak, centered at approximately 705 nm and corresponding to a photon energy of 1.75 eV, is visible in all compositions. This indicates that the emission processes of the material are deep-level or linked to flaws. The following relation (6) was used to calculate the optical photon energy:

$$E = 1240/\lambda \quad (6)$$

where "λ" is the emission wavelength in nanometers and "E" is the photon excitation energy in electron volts. This red-region emission can be attributed to the radiative recombination of electrons from defect states or transitions involving centers in the spinel lattice sites.[43,44]

On the other hand, the black curve, showing the pure $SnFe_2O_4$ sample, has the lowest PL intensity, highlighting how Cr^{2+} ions affect the optical emission of the ferrite system due to the degree of polarization.[45] The steady increase in PL intensity

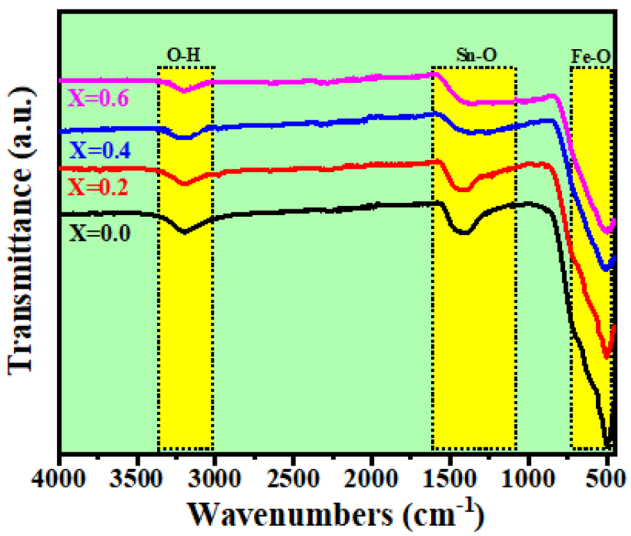

Fig. 3 FTIR spectra of the $Sn_{1-x}Cr_xFe_2O_4$ (where x = 0.00, 0.20, 0.40, and 0.60) spinel ferrites.

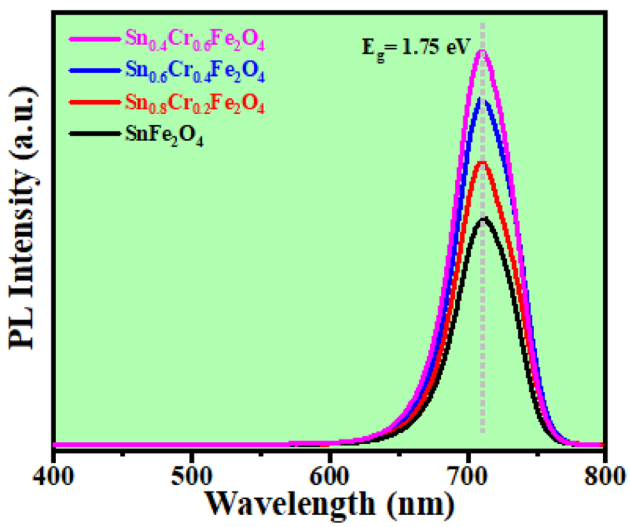

Fig. 4 PL spectra of the $Sn_{1-x}Cr_xFe_2O_4$ (where x = 0.00, 0.20, 0.40, and 0.60) spinel ferrites.

with increasing Cr^{2+} points to improved defect density and electronic transitions associated with Cr^{2+} trap states. The emission peaks do not change much, suggesting that the dopant mostly modifies the recombination rate rather than the energy levels. The consistent rise in PL intensity with Cr^{2+} content suggests better defect density and electronic transitions involving Cr^{2+}-related trap states. The positions of the emission peaks remain rather consistent, indicating that the dopant does not significantly alter the energy levels but rather primarily affects the recombination rate.[46] These findings validate that the electrical band structure and defect states are altered by Cr^{2+} doping, improving the luminescence characteristics of $SnFe_2O_4$ spinel ferrites. Due to these characteristics, these doped ferrites could be used in photonic and optoelectronic device applications.[18]

4.3 Ultra violet-visible (UV-vis) spectrophotometry

UV-vis spectrophotometry is a valuable technique for analyzing the optical behavior and calculating the band gap energy of spinel ferrite materials. Fig. 5(a) and (b) show the absorbance spectra and band gap energy of pure and Cr^{2+}-doped $SnFe_2O_4$ ferrite materials, respectively. All samples show strong absorption in the UV region (<400 nm), attributed to charge transfer transitions between O^{2-} (2p) and Fe^{3+} (3d) ions in the spinel structure. As the Cr^{2+} doping concentration increases from $x = 0.00$ to $x = 0.60$, a noticeable red shift in the absorption edge is observed, suggesting a reduction in the optical band gap energy. This variation in the absorption edge suggests that Cr^{2+} ions, when integrated into the $SnFe_2O_4$ lattice, affect the electronic band structure. Because Cr^{2+} has a different ionic radius (0.73 Å) than Sn^{2+} (1.22 Å), it disturbs the Sn–O–Sn super exchange interaction and causes local distortion in the tetrahedral coordination, which alters the bandwidth and creates localized defect states or impurity bands within the forbidden gap, lowering the transition energy needed for electron excitation.[47,48]

The optical band gap energies (E_g) of all compositions were calculated by using the Tauc relation:[49]

$$(\alpha h\nu)^2 = A(h\nu - E_g) \quad (7)$$

where 'α' is the absorption coefficient, '$h\nu$' is the photon energy, 'A' is a constant, and 'E_g' is the band gap energy. The E_g values were calculated by extrapolating the linear region in the Tauc plot (Fig. 5(b)) to the energy axis at $(\alpha h\nu)^2 = 0$.

The plots of $t(\alpha h\nu)^2$ *versus* bandgap energy (E_g) are shown in Fig. 5(b). The linear portion of each curve was extrapolated to the energy axis to determine the corresponding band gap values. The obtained values for the synthesized ferrite samples are mentioned in Table 2.

This monotonic decrease in band gap energy with Cr^{2+} doping can be attributed to the following factors:

(i) Cr^{2+} ions may introduce defect states within the band gap, facilitating lower-energy transitions.

(ii) Doping-induced lattice distortion affects the Fe–O and Cr–O bond lengths, modifying the crystal field and reducing the separation between the valence and conduction bands.

(iii) Cr^{2+} has partially filled 3d orbitals that can hybridize with O 2p orbitals, leading to narrowing of the band gap.

Such tunability in the optical band gap makes Cr^{2+}-doped $SnFe_2O_4$ spinel ferrites suitable candidates for visible-light-driven photocatalysis, solar cell absorbers, and other optoelectronic applications. These findings align well with previous reports on Cr^{2+}-doped ferrite systems, such as $ZnFe_2O_4$ and $NiFe_2O_4$, where similar redshifts and band gap reductions were observed upon Cr^{2+} substitution due to the formation of intermediate energy states and enhanced d–d transitions.[50–52] The

Table 2 Band gap energies of the $Sn_{1-x}Cr_xFe_2O_4$ (where $x = 0.00$, 0.20, 0.40, and 0.60) spinel ferrites

S. no.	Contents (x)	Optical band gap energy (eV)
1	0.00	2.53 eV
2	0.20	2.45 eV
3	0.40	2.38 eV
4	0.60	2.32 eV

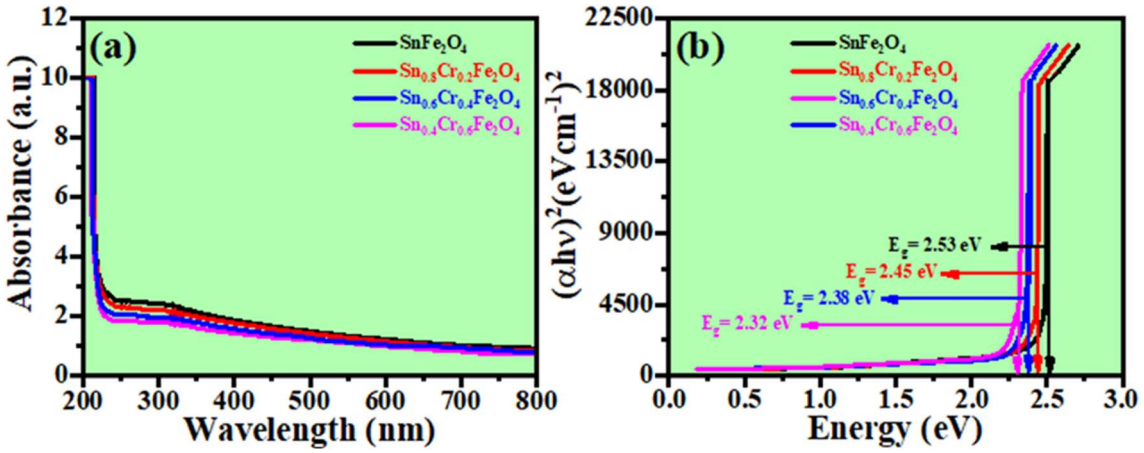

Fig. 5 (a) Absorbance spectra and (b) band gap energy of the $Sn_{1-x}Cr_xFe_2O_4$ (where $x = 0.00$, 0.20, 0.40, and 0.60) spinel ferrites.

optical band gap obtained from UV-vis absorption (2.32–2.58 eV) represents the fundamental interband transition from the valence band to the conduction band. The lower energy emission peak observed in the PL spectra (~1.75 eV) arises from defect-mediated radiative recombination. This discrepancy is attributed to sub-band gap states introduced by Cr doping, such as Fe^{2+}/Fe^{3+} and Cr^{2+}/Cr^{3+} localized levels, which act as recombination centers. Electrons excited to the conduction band can relax to these defect states before recombining radiatively with holes, thereby producing PL emission at lower energies than the fundamental band gap.[34,37,40]

5. Dielectric and electrical properties

5.1 Dielectric constant

The frequency-dependent dielectric constants (ε_r) of $Sn_{1-x}Cr_xFe_2O_4$ (where $x = 0.00$, 0.20, 0.40, and 0.60) are shown in Fig. 6. All compositions exhibited similar dielectric dispersion behaviors, characterized by a steep decline in ε_r with increasing frequency, followed by stabilization at higher frequencies.[53]

At lower frequencies (<0.1 MHz), the dielectric constant is relatively high. It can be attributed to interfacial (Maxwell–Wagner) polarization and space charge accumulation at grain boundaries, as explained by Koop's phenomenological theory.[54] In ferrite systems, the microstructure plays a vital role: large grain boundaries can trap more charges, leading to higher polarization. The decrease in ε_r with frequency is due to the inability of charge carriers to follow the alternating field at higher frequencies, reducing their contribution to polarization. As the Cr^{2+} doping concentration increases, ε_r increases significantly at all frequencies. This trend indicates that Cr^{2+} ions effectively enhance the dielectric response of $SnFe_2O_4$. Several factors contribute to this enhancement:

(i) Cr is doped into the $SnFe_2O_4$ spinel lattice, primarily substituting Sn^{2+} ions, but partial occupation of Fe^{3+} sites cannot be excluded.

(ii) SEM and XRD results often reveal that Cr^{2+} doping can refine the grain size, increasing the density of grain boundaries and promoting interfacial polarization.[26]

(iii) Cr^{2+} doping may distort the lattice due to ionic radius mismatch, introducing additional dipolar moments that increase dielectric polarization.[55]

(iv) Doping can improve densification during sintering, reducing porosity and enhancing dielectric pathways.

For every sample, ε_r became almost constant at higher frequencies (>1 MHz). Electronic and ionic polarization processes, which are more frequency stable and less frequency-dependent, dominate this plateau region.[56] The observed dielectric behavior is mostly interfacial in nature, as confirmed by the diminished impact of space charge polarization at this point. An adjustable dielectric response is suggested by the general increase in dielectric constant with Cr^{2+} content, which makes Cr-doped $SnFe_2O_4$ a viable material for use in memory storage systems, microwave devices, and high-frequency capacitors.

5.2 Tangent loss

Fig. 7 shows the variation of dielectric loss ($\tan\delta$) with frequency in the range of 0.01–2 MHz for the $Sn_{1-x}Cr_xFe_2O_4$ (where $x = 0.00$, 0.20, 0.40, and 0.60) spinel ferrites. All samples show usual dielectric relaxation behavior, with a steep drop in loss at low frequencies, followed by a nearly constant value at higher frequencies.

At lower frequencies (less than 0.1 MHz), $\tan\delta$ is significantly high, with values exceeding 5 for the undoped $SnFe_2O_4$ ferrite. This behavior is attributed to space charge polarization and conductive losses arising from interfacial effects.[57]

Tan δ values drop quickly as the frequency rises, eventually plateauing at a minimum. This drop suggests that there are fewer energy losses because the dipoles or charge carriers are unable to follow the high-frequency field oscillations. All

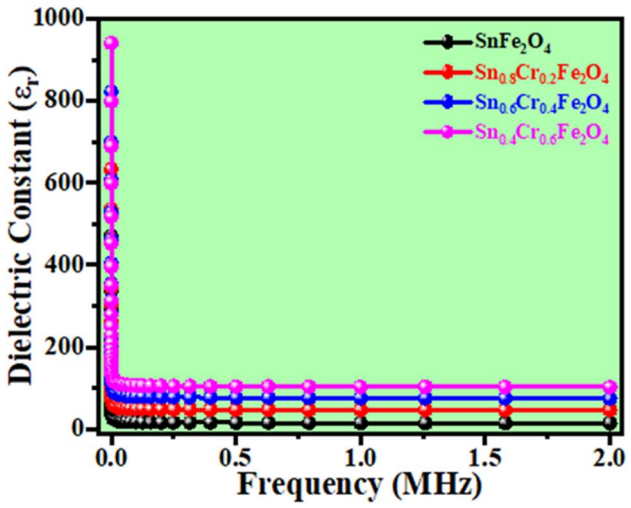

Fig. 6 Variation in ε_r with frequency of the $Sn_{1-x}Cr_xFe_2O_4$ (where $x = 0.00$, 0.20, 0.40, and 0.60) spinel ferrites.

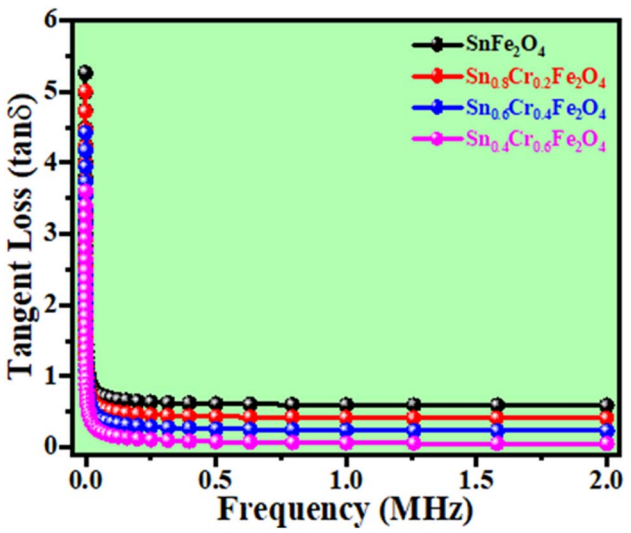

Fig. 7 Variation in $\tan\delta$ with frequency of the $Sn_{1-x}Cr_xFe_2O_4$ (where $x = 0.00$, 0.20, 0.40, and 0.60) spinel ferrites.

samples showed stable, low tan δ values above 0.5 MHz, suggesting enhanced dielectric efficiency at high frequencies.

The following factors were observed for the $Sn_{1-x}Cr_xFe_2O_4$ (where $x = 0.00$, 0.20, 0.40, and 0.60) spinel ferrites:

(i) The substitution of Cr^{2+} into the $SnFe_2O_4$ lattice leads to a reduction in tan δ across all frequency ranges. This effect becomes more pronounced at higher Cr^{2+} concentrations ($x = 0.60$), where tan δ drops below 1 at 1 MHz.

(ii) Cr^{2+} doping is known to improve microstructure by refining the grain size and increasing the grain boundary density. These grain boundaries act as barrier layers, suppressing long-range charge motion and thereby reducing energy loss.[36]

(iii) Cr^{2+} ions can enhance the electrical resistivity of the ferrite matrix, effectively suppressing leakage currents and minimizing tangent losses.

These observations confirm that Cr^{2+} doping is effective in minimizing tan δ, especially at higher frequencies, thus enhancing the material's applicability in microwave and high-frequency device applications.

5.3 AC conductivity

The frequency-dependent AC conductivities (σ_{ac}) of the $Sn_{1-x}Cr_xFe_2O_4$ (where $x = 0.00$, 0.20, 0.40, and 0.60) spinel ferrites are shown in Fig. 8. All samples show a monotonic increase in conductivity with frequency, indicating typical semiconductor-like behavior and supporting the correlated barrier hopping conduction model.[58] Grain boundaries that act as potential barriers and impede charge carrier mobility cause the conductivity to be significantly lower at lower frequencies. The localized charge carriers acquire enough energy to jump between nearby locations as the frequency increases, which raises σ_{ac}. The frequency-dependent behavior can be expressed by the Jonscher power law:

$$\sigma_{ac}(f) = \sigma_{dc} + Af^n \quad (8)$$

where 'σ_{dc}'is the frequency-independent DC conductivity, 'A' is a free factor, 'f' is the applied frequency, and 'n' is the frequency exponent, *i.e.*, ($0 < n < 1$), which indicates the conduction mechanism.

From the σ_{ac} plot, the pure $SnFe_2O_4$ exhibits the highest ac conductivity, while the sample with $x = 0.60$ shows the lowest. This decreasing σ_{ac} with Cr^{2+} concentration can be ascribed to the suppression of the polaron hopping mechanism. The tangent loss and leakage current were reduced due to the lower conductivity, which might be helpful for dielectric applications.

5.4 Nyquist plot analysis

An impedance analyzer is a potent tool for exploring the electrical response and charge carrier transportation mechanisms in spinel ferrites. The Nyquist plots (Z'' *vs.* Z') for $Sn_{1-x}Cr_xFe_2O_4$ (where $x = 0.00$, 0.20, 0.40, and 0.60) spinel ferrites, shown in Fig. 9, exhibit a single semicircular arc for each composition, indicating the dominant contribution of the grain (bulk) effect to the total impedance. The absence of additional arcs suggests a negligible grain boundary or electrode effects within the measured frequency range. It was found that the arc radius systematically decreases with increasing Cr^{2+} doping concentration, indicating a significant reduction in bulk resistance and enhancement in electrical conductivity. The real part of the impedance (Z') represents the resistance provided by the material, while the imaginary part (Z'') is linked to the reactance component and relaxation processes. The undoped $SnFe_2O_4$ composition showed the highest bulk resistance (~6.5 kΩ), while the composition at $x = 0.60$ showed the lowest impedance (~3.5 kΩ), as seen by the intersection of the arc with the Z' axis. This decreasing trend in Z' and Z'' values may be due to the Cr^{2+} substitution effect, mixed valency, and grain conductivity mechanism.

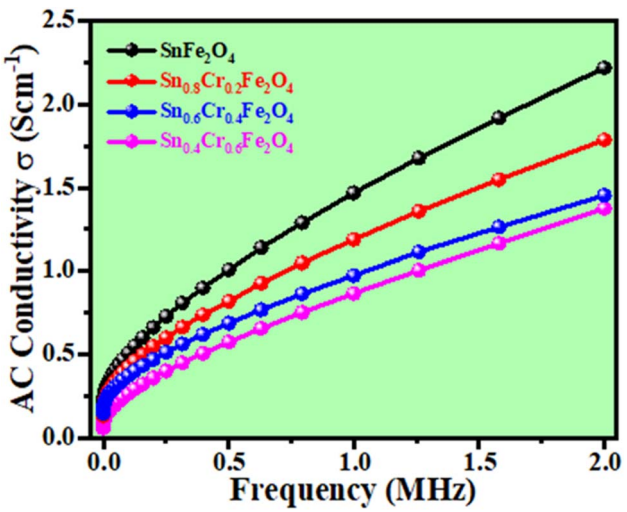

Fig. 8 Variation in σ_{ac} with frequency of the $Sn_{1-x}Cr_xFe_2O_4$ (where $x = 0.00$, 0.20, 0.40, and 0.60) spinel ferrites.

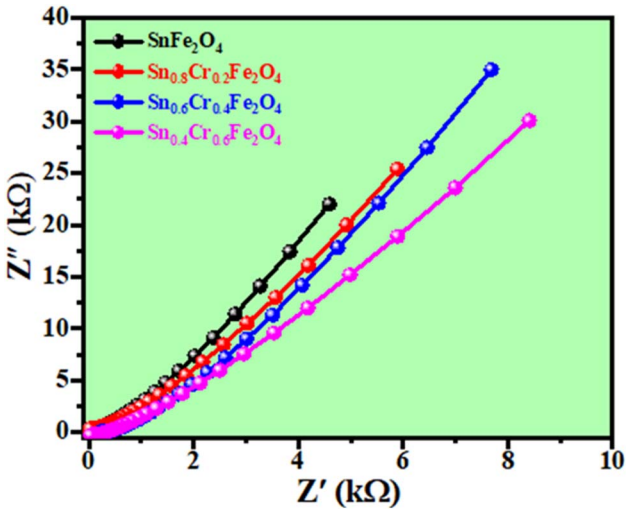

Fig. 9 Variation in the imaginary impedance (Z'') with the real impedance (Z') of the $Sn_{1-x}Cr_xFe_2O_4$ (where $x = 0.00$, 0.20, 0.40, and 0.60) spinel ferrites.

5.5 Frequency-dependent modulus spectrum

Fig. 10 shows the variation of the electrical modulus (M) with the frequency of the $Sn_{1-x}Cr_xFe_2O_4$ (where $x = 0.00$, 0.20, 0.40, and 0.60) spinel ferrites. The electrical modulus provides critical insights into the electrical relaxation phenomena and helps isolate the grain and grain boundary contributions in crystalline materials. It is defined by the reciprocal of the complex permittivity (ε^*):

$$M = 1/\varepsilon^* = M' + jM'' \quad (9)$$

where M' is the real part, while M'' is the imaginary part of the modulus. The electric modulus formalism is an essential approach for investigating the dielectric relaxation behavior and charge transport phenomena in ferrite materials. The electric modulus study revealed that Cr^{2+} substitution in $SnFe_2O_4$ significantly influences the dielectric relaxation behavior. The modulus decreases with doping, indicating enhanced electrical conductivity and less polarization effects, two important properties for use in sensors, memory devices, and spintronic components. For all samples, the modulus decreases sharply with increasing frequency and tends to approach zero at high frequencies (>4.5 kHz), indicating the long-range mobility of charge carriers at low frequencies and localized relaxation at higher frequencies.

6 Conclusion

This study comprehensively clarifies how the structural, optical, vibrational, and dielectric properties of the $Sn_{1-x}Cr_xFe_2O_4$ (where $x = 0.00$, 0.20, 0.40, and 0.60) spinel ferrites manufactured using a standard method are affected. Due to the substitution of the smaller Cr^{2+} ions (0.73 Å) at the larger Sn^{2+} (1.22 Å) cation sites, XRD patterns verified the creation of a single-phase cubic structure with space group ($Pn\bar{3}$), with a steady decrease in lattice parameters and crystallite size. Increased lattice strain and microstructural distortion were also suggested by the observed peak broadening and shift after doping. The FTIR spectra exhibit multiple absorption bands that confirm the formation of a spinel ferrite structure. PL emission spectra were observed at a 705 nm wavelength, and the optical photon energy is 1.75 eV, which is useful for the production of red lasers. Optical absorption spectra revealed a progressive decrease in the band gap energy from 2.53 eV to 2.32 eV, indicating decreased charge carrier localization. Both the dielectric constant (ε_r) and the tangent loss ($\tan\delta$) showed considerable dispersion at lower frequencies, stabilizing at higher frequencies, in a typical Maxwell–Wagner type interfacial polarization mechanism, according to dielectric research. Improved resistive grain boundary behavior and less space charge polarization were indicated by a significant decrease in $\tan\delta$ and an improvement in frequency stability as the concentration of Cr^{2+} increased. As the Cr^{2+} content rises, the σ_{ac} falls, further reducing the leakage current and tangent loss. The decrease in modulus with doping suggests improved electrical conductivity and reduced polarization effects. These tunable multifunctional properties render Cr^{2+}-doped $SnFe_2O_4$ a potential candidate for applications in memory devices, sensors, spintronic components, optoelectronics, high-frequency dielectric components, photoelectronic devices, and spinel-based multifunctional ceramics.

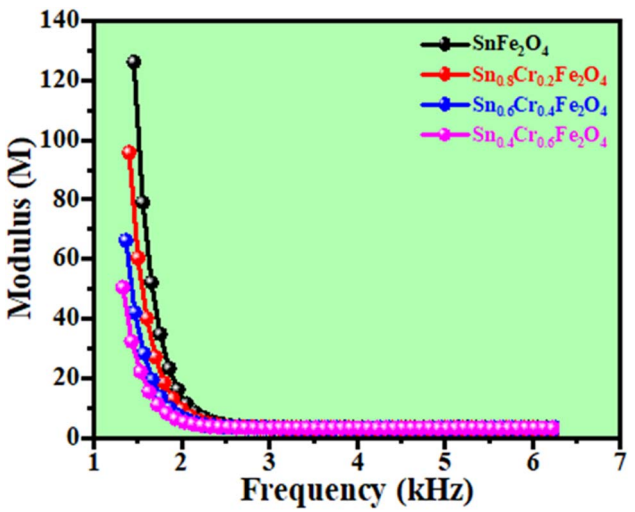

Fig. 10 Variation in the electrical modulus (M) with frequency of the $Sn_{1-x}Cr_xFe_2O_4$ (where $x = 0.00$, 0.20, 0.40, and 0.60) spinel ferrites.

Conflicts of interest

The authors declare no conflict of interest.

Data availability

The data will be made available on reasonable request.

Acknowledgements

The authors extend their appreciation to the Deanship of Research and Graduate Studies at King Khalid University, Kingdom of Saudi Arabia, for funding this work through the Large Research Group Project under the grant number RGP.2/198/46. The authors extend their appreciation to the Deanship of Scientific Research at Northern Border University, Arar, KSA, for funding this research work through the project number "NBU-FFMRA-2025-2483-06".

References

1 D. Seetharaman, Investigation of thermal stability, structure, magnetic and dielectric properties of solvothermally synthesised SnFe2O4, *Open Ceram.*, 2022, **9**, 100222.
2 G. Sedaghati-Jamalabad and M. M. Bagheri-Mohagheghi, A study on the structural and optical properties of the SnFe2O4 spinel compound as anode electrode in Li ion-battery: the optical and dielectric parameters via synthesis methods, *Opt. Quantum Electron.*, 2024, **56**(6), 965.

3 O. Mounkachi, M. Hamedoun and A. Benyoussef, Electronic and magnetic properties of SnFe2O4 spinel ferrites, *J. Supercond. Novel Magn.*, 2017, **30**(11), 3035–3038.
4 A. Shokri, S. F. Shayesteh and K. Boustani, The role of Co ion substitution in SnFe2O4 spinel ferrite nanoparticles: study of structural, vibrational, magnetic and optical properties, *Ceram. Int.*, 2018, **44**(18), 22092–22101.
5 G. Sedaghati-Jamalabad and M. M. Bagheri-Mohagheghi, The influence of rGO and GO nano plates on structural, optical and magnetic properties of SnFe2O4 nanocomposites synthesised by sol–gel, microwave and co-precipitation methods, *J. Mater. Sci.: Mater. Electron.*, 2024, **35**(23), 1554.
6 G. Sedaghati-Jamalabad and M. M. Bagheri-Mohagheghi, High specific surface area (2840.3 m2/g) in activated carbon/SnFe2O4 spinel nanocomposite: structural, optical, dielectric, and magnetic properties for Li-ion battery soft and porous electrode applications, *Appl. Phys. A:Mater. Sci. Process.*, 2024, **130**(9), 645.
7 H. Han, Y. Luo, Y. Jia, N. Hasan and C. Liu, A review on SnFe2O4 and their composites: Synthesis, properties, and emerging applications, *Prog. Nat. Sci.:Mater. Int.*, 2022, **32**(5), 517–527.
8 A. B. Bhosale, S. B. Somvanshi, V. D. Murumkar and K. M. Jadhav, Influential incorporation of RE metal ion (Dy^{3+}) in yttrium iron garnet (YIG) nanoparticles: magnetic, electrical and dielectric behaviour, *Ceram. Int.*, 2020, **46**(10), 15372–15378.
9 Q. Mahmood, B. U. Haq, M. Rashid, N. A. Noor, S. AlFaify and A. Laref, First-principles study of magnetic and thermoelectric properties of SnFe2O4 and SnCo2O4 spinels, *J. Solid State Chem.*, 2020, **286**, 121279.
10 R. Lamouri, M. Tadout, M. Hamedoun, A. Benyoussef, H. Ez-Zahraouy, M. Benaissa and O. Mounkachi, Effect of the cations distribution on the magnetic properties of SnFe2O4: First-principles study, *J. Magn. Magn. Mater.*, 2017, **436**, 6–10.
11 R. K. Gupta, K. Ghosh and P. K. Kahol, Structural and magnetic properties of epitaxial SnFe2O4 thin films, *Mater. Lett.*, 2011, **65**(14), 2149–2151.
12 Z. Yang, S. Huo, Z. Zhang, F. Meng, B. Liu, Y. Wang, Y. Ma, Z. Wang, J. Xu, Q. Tian and Y. Wang, High-Precision Multibit Opto-Electronic Synapses Based on ReS2/h-BN/Graphene Heterostructure for Energy-Efficient and High-Accuracy Neuromorphic Computing, *Adv. Funct. Mater.*, 2025, 2509119.
13 O. Mounkachi, L. Fkhar, R. Lamouri, E. Salmani, M. Hamedoun, H. Ez-Zahraouy, E. K. Hlil, M. Ait Ali and A. Benyoussef, Magnetic properties and magnetoresistance effect of SnFe2O4 spinel nanoparticles: Experimental, ab initio and Monte Carlo simulation, *Ceram. Int.*, 2021, **47**(22), 31886–31893.
14 C. Zhang, Y. Dong, P. Hu, H. Fu, H. Yang, R. Yang, Y. Dong, L. Zou and J. Tan, Large-range displacement measurement in narrow space scenarios: fiber microprobe sensor with subnanometer accuracy, *Photonics Res.*, 2024, **12**(9), 1877–1889.
15 G. Sedaghati-Jamalabad and M. M. Bagheri-Mohagheghi, Influence of synthesis route on structural properties of SnFe2O4 spinel phase via methods of co-precipitation, sol–gel and solvothermal: morphology, phase analysis, crystallite size and lattice strain, *Discover Appl. Sci.*, 2024, **6**(4), 202.
16 C. Li, X. Chen, Z. Zhang, X. Wu, T. Yu, R. Bie, D. Yang, Y. Yao, Z. Wang and L. Sun, Charge-selective 2D heterointerface-driven multifunctional floating gate memory for in situ sensing-memory-computing, *Nano Lett.*, 2024, **24**(47), 15025–15034.
17 M. Ashan, H. A. Alyousef, A. W. Alrowaily, B. M. Alotaibi, N. Al-Harbi, H. H. Somaily, M. Aslam, K. Ahmad and S. Aman, Maximizing the electrochemical efficiency of Ce doped SnFe2O4 through hydrothermal route for supercapacitor applications, *Electrochim. Acta*, 2024, **504**, 144840.
18 M. Shaterian, H. H. Ardeshiri, R. Mohammadi, Z. Aghasadeghi and M. Karami, RETRACTED: Synthesis, characterization, and electrochemical evaluation of SnFe2O4@ MWCNTS nanocomposite as a potential hydrogen storage material, *Heliyon*, 2023, **9**(6), e16648.
19 Y. Guan, L. Yang, C. Chen, R. Wan, C. Guo and P. Wang, Regulable crack patterns for the fabrication of high-performance transparent EMI shielding windows, *Iscience*, 2025, **28**(1), 111543.
20 F. G. El Desouky, M. M. Saadeldin and W. H. Eisa, Synergistic influence of SnFe2O4 on ZnSnO3 hybrid nanostructures and optimizations optical, photoluminescence, and magnetic properties for multifunction application, *Surf. Interfaces*, 2023, **38**, 102749.
21 M. T. Sebastian, *Dielectric Materials for Wireless Communication*, Elsevier, 2010.
22 A. Ali, A. Zaman, A. H. Jabbar, V. Tirth, A. Algahtani, A. Alhodaib, I. Ullah, J. S. Ahmed and M. Aljohani, Effects of strontium on the structural, optical, and microwave dielectric properties of Ba2Ti9O20 ceramics synthesized by a mixed oxide route, *ACS Omega*, 2022, **7**(29), 25573–25579.
23 A. Algahtani, S. Ali, T. Hussain, A. Ali, A. M. Quraishi, V. Tirth, B. S. Abdullaeva, M. Kamran, M. Aslam and A. Zaman, Studies on structural, optical and microwave dielectric properties of double perovskite Sr2Fe1+ xNb1-xO6, ceramics synthesized by solid state route, *Opt. Mater.*, 2024, **148**, 114822.
24 A. Ali, A. Zaman, M. K. Khan, L. B. Farhat, A. H. Jabbar, K. M. Badi, I. Ullah, V. Tirth and S. Khan, Structural Evaluation, Optical, and Dielectric Properties of Ba-Doped Ca4Ti3O10-Sintered Ceramics, *J. Supercond. Novel Magn.*, 2022, **35**(7), 1987–1993.
25 G. Zhang, Z. Hou, P. Zhao, M. Chao, Z. Li, X. Zhao, Y. Lu and X. Zhang, Visible light response SnFe2O4/BiOCl microspheres: Sysnthesis, magnetical and photocatalytic properties, *J. Alloys Compd.*, 2024, **1008**, 176732.
26 A. Ali, S. Uddin, Z. Iqbal, M. Lal and A. Zaman, Structural, optical and microwave dielectric properties of barium tetra titanate (BaTi4O9) ceramics, *J. Optoelectron. Adv. Mater.*, 2021, **23**(1–2), 48–52.

27 M. T. Sebastian, *Dielectric Materials for Wireless Communication*, Elsevier, 2010.
28 G. L. Zhang, C. F. Pan, Y. H. Sun, J. L. Wei, D. C. Guan and J. M. Nan, Synergistic effects of flake-like ZnO/SnFe2O4/nitrogen-doped carbon composites on structural stability and electrochemical behavior for lithium-ion batteries, *J. Colloid Interface Sci.*, 2021, **594**, 173–185.
29 V. K. Raut, S. B. Somvanshi, E. A. Dawi and C. T. Birajdar, Facile sol–gel synthesis of trivalent Al3+-Gd3+ ions co-doped nanoscale cobalt spinel ferrite for magneto-electronic applications, *Inorg. Chem. Commun.*, 2024, **168**, 112907.
30 P. P. Babu, Structural and magnetic study of chromium ferrite nanoparticles, *Mater. Sci.*, 2020, **19**(02), 751–755.
31 B. Dash, K. L. Routray, S. Saha, M. K. Rout, S. Sarangi and P. M. Sarun, Cr-modified CoFe2O4 nano ferrites: a study of structural, morphological, electrical, dielectric, magnetic and magneto dielectric evolution, *Appl. Phys. A:Mater. Sci. Process.*, 2025, **131**(1), 5.
32 R. S. Rajenimbalkar, S. S. Ghuge, V. J. Deshmukh, E. A. Dawi and S. B. Somvanshi, Effect of Zn2+–Ti4+ co-doping on the structural, infrared, surface, magnetic, electric and dielectric parameters of nanoscale CoFe2O4, *J. Mater. Sci.: Mater. Electron.*, 2024, **35**(27), 1789.
33 M. B. Shafqat, M. Ali, S. Atiq, S. M. Ramay, H. M. Shaikh and S. Naseem, Structural, morphological and dielectric investigation of spinel chromite (XCr2O4, X= Zn, Mn, Cu & Fe) nanoparticles, *J. Mater. Sci.: Mater. Electron.*, 2019, **30**(19), 17623–17629.
34 A. Parveez, M. S. Shekhawat, S. Sindhu, C. Srikanth, F. Nayeem, M. S. S, R. R. Sinha, A. Chaudhuri, and S. A. Khader, Dielectric and magnetic studies of Cr+ 3 doped nickel ferrite by combustion method, in *AIP Conference Proceedings*, 2018, vol. 1953(1), p. 030283.
35 P. M. Visakh, Preparations, Characterization, and Applications of Multiferroic Nanocomposites, *Nanostruct. Multiferroics*, 2021, 233–247.
36 A. Ali, M. Irfan, M. N. Akhtar, T. A. Sheikh, M. Ramzan, S. Ullah, M. Al Huwayz, A. S. Alshomrany, M. S. Al-Buriahi, G. A. Ashraf and M. A. Khan, Cr-doped Li-based β-(Beta) type hexaferrites: XRD, FTIR, XPS and dielectric evaluations for high-frequency applications, *Mater. Chem. Phys.*, 2024, **327**, 129873.
37 S. B. Somvanshi and E. A. Dawi, Sol–gel synthesized nanoscale mixed Zn-Mg ferrite as nanoseeds for in vitro magnetic fluid hyperthermia for cancer treatment, *J. Sol-Gel Sci. Technol.*, 2025, **19**, 1–12.
38 E. K. Senbeto and S. Elangovan, Effects of chromium (III) ion doping on structural, optical, and magnetic properties of nickel–cobalt ferrite nanoparticle, *J. Nanomater.*, 2023, **2023**(1), 5103278.
39 Y. Jiang, M. Wang, L. Zhang, S. Liu, Y. Cao, S. Qian, Y. Cheng, X. Xu, C. Yan and T. Qian, Distorted spinel ferrite heterostructure triggered by alkaline earth metal substitution facilitates nitrogen localization and electrocatalytic reduction to ammonia, *Chem. Eng. J.*, 2022, **450**, 138226.
40 K. Luo, Q. Fu, X. Liu, R. Zhao, Q. He, B. Hu, Z. An, W. Yang, Y. Zhang, S. Zhang and J. Zhan, Study of polarization transmission characteristics in nonspherical media, *Opt Laser. Eng.*, 2024, **174**, 107970.
41 M. A. Ansari, A. Baykal, S. Asiri and S. Rehman, Synthesis and characterization of antibacterial activity of spinel chromium-substituted copper ferrite nanoparticles for biomedical application, *J. Inorg. Organomet. Polym. Mater.*, 2018, **28**(6), 2316–2327.
42 S. Y. Mulushoa, C. V. Kumari, V. Raghavendra, K. E. Babu, B. S. Murthy, K. Suribabu, Y. Ramakrishna and N. Murali, Effect of Zn–Cr substitution on the structural, magnetic and electrical properties of magnesium ferrite materials, *Phys. B*, 2019, **572**, 139–147.
43 K. Maaz, S. Karim, A. Mumtaz, S. K. Hasanain, J. Liu and J. L. Duan, Synthesis and magnetic characterization of nickel ferrite nanoparticles prepared by co-precipitation route, *J. Magn. Magn. Mater.*, 2009, **321**(12), 1838–1842.
44 S. Debnath and R. Das, Study of the optical properties of Zn doped Mn spinel ferrite nanocrystals shows multiple emission peaks in the visible range–a promising soft ferrite nanomaterial for deep blue LED, *J. Mol. Struct.*, 2020, **1199**, 127044.
45 V. K. Raut, S. B. Somvanshi, E. A. Dawi and C. T. Birajdar, Sol-gel auto combustion synthesis of Al3+-Gd3+ ions co-doped cobalt ferrite nanoparticles for nanoelectronics applications, *J. Sol-Gel Sci. Technol.*, 2024, **112**(3), 738–751.
46 M. A. Rafiq, A. Javed, M. N. Rasul, M. A. Khan and A. Hussain, Understanding the structural, electronic, magnetic and optical properties of spinel MFe2O4 (M= Mn, Co, Ni) ferrites, *Ceram. Int.*, 2020, **46**(4), 4976–4983.
47 H. Lemziouka, A. Boutahar, R. Moubah, L. H. Omari, S. Bahhar, M. Abid and H. Lassri, Synthesis, structural, optical and dispersion parameters of La-doped spinel zinc ferrites ZnFe2-xLaxO4 (x= 0.00, 0.001, 0.005, 0.01 and 0.015), *Vacuum*, 2020, **182**, 109780.
48 M. M. Sonia, S. Anand, V. M. Vinosel, M. A. Janifer, S. Pauline and A. Manikandan, Effect of lattice strain on structure, morphology and magneto-dielectric properties of spinel $NiGd_xFe_{2-x}O_4$ ferrite nano-crystallites synthesized by sol-gel route, *J. Magn. Magn. Mater.*, 2018, **466**, 238–251.
49 D. Harrabi, S. Hcini, J. Dhahri, M. A. Wederni, A. H. Alshehri, A. Mallah, K. Khirouni and M. L. Bouazizi, Study of structural and optical properties of Cu–Cr substituted Mg–Co spinel ferrites for optoelectronic applications, *J. Inorg. Organomet. Polym. Mater.*, 2023, **33**(1), 47–60.
50 R. S. Rajenimbalkar, V. J. Deshmukh, K. K. Patankar and S. B. Somvanshi, Effect of multivalent ion doping on magnetic, electrical, and dielectric properties of nickel ferrite nanoparticles, *Sci. Rep.*, 2024, **14**(1), 29547.
51 S. Singhal, S. Jauhar, J. Singh, K. Chandra and S. Bansal, Investigation of structural, magnetic, electrical and optical properties of chromium substituted cobalt ferrites (CoCrxFe2− xO4, 0≦ x≦ 1) synthesized using sol gel auto combustion method, *J. Mol. Struct.*, 2012, **1012**, 182–188.
52 M. A. Amer, A. Matsuda, G. Kawamura, R. El-Shater, T. Meaz and F. Fakhry, Structural, magnetic, vibrational and optical

studies of structure transformed spinel Fe2+-Cr nanoferrites by sintering process, *J. Alloys Compd.*, 2018, **735**, 975–985.

53 D. Yang, Y. Lin, W. Meng, Z. Wang, H. Li, C. Li, Z. Zhang, Q. Zhang, J. You, J. Wang and T. Yu, Relaxor Antiferroelectric Dynamics for Neuromorphic Computing, *Adv. Mater.*, 2025, **24**, 2419204.

54 M. M. Mubasher, M. Hassan, L. Ali, Z. Ahmad, M. A. Imtiaz, M. F. Aamir, A. Rehman and K. Nadeem, Comparative study of frequency-dependent dielectric properties of ferrites MFe2O4 (M= Co, Mg, Cr and Mn) nanoparticles, *Appl. Phys. A:Mater. Sci. Process.*, 2020, **126**(5), 334.

55 M. B. Shafqat, M. Ali, S. Atiq, S. M. Ramay, H. M. Shaikh and S. Naseem, Structural, morphological and dielectric investigation of spinel chromite (XCr2O4, X= Zn, Mn, Cu & Fe) nanoparticles, *J. Mater. Sci.: Mater. Electron.*, 2019, **30**(19), 17623–17629.

56 F. Hcini, S. Hcini, M. A. Wederni, B. Alzahrani, H. Al Robei, K. Khirouni, S. Zemni and M. L. Bouazizi, Structural, optical, and dielectric properties for Mg0· 6Cu0· 2Ni0· 2Cr2O4 chromite spinel, *Phys. B*, 2022, **624**, 413439.

57 A. V. Humbe, S. B. Somvanshi, J. S. Kounsalye, A. Kumar and K. M. Jadhav, Influential trivalent ion (Cr3+) substitution in mixed Ni–Zn nanoferrites: Cation distribution, magnetic, Mossbauer, electric, and dielectric studies, *Ceram. Int.*, 2022, **48**(22), 34075–34083.

58 S. B. Somvanshi, S. A. Jadhav, M. V. Khedkar, P. B. Kharat, S. D. More and K. M. Jadhav, Structural, thermal, spectral, optical and surface analysis of rare earth metal ion (Gd3+) doped mixed Zn–Mg nano-spinel ferrites, *Ceram. Int.*, 2020, **46**(9), 13170–13179.